Article

Grain Engineering for Perovskite/Silicon Monolithic Tandem Solar Cells with Efficiency of 25.4%

Bo Chen, Zhengshan Yu, Kong Liu, ..., Peter N. Rudd, Zachary Holman, Jinsong Huang

zachary.holman@asu.edu (Z.H.)
jhuang@unc.edu (J.H.)

HIGHLIGHTS

Synergistic effects of additives create large grains and low defect density

1.80 V tandem device enabled by a 1.64-eV perovskite with V_{oc} deficit of 0.49 V

25.4%-efficient monolithic perovskite/Si tandem device

Grain engineering through combined MACl and MAH_2PO_2 additives in perovskite precursors improves the photovoltaic performance of perovskite/silicon tandem cells. MACl increases the grain size of wide-bandgap perovskite films and also produces smooth films. MAH_2PO_2 suppresses non-radiative recombination sites at grain boundaries. The synergetic effects of MACl and MAH_2PO_2 further promote grain growth and prolong the carrier recombination lifetime. This enables a power conversion efficiency of 25.4% for a perovskite/silicon tandem device.

Article

Grain Engineering for Perovskite/Silicon Monolithic Tandem Solar Cells with Efficiency of 25.4%

Bo Chen,[1,2,5] Zhengshan Yu,[3,5] Kong Liu,[1,4,5] Xiaopeng Zheng,[1] Ye Liu,[1] Jianwei Shi,[3] Derek Spronk,[2] Peter N. Rudd,[2] Zachary Holman,[3,*] and Jinsong Huang[1,2,6,*]

SUMMARY

Organic-inorganic halide perovskites are promising semiconductors to mate with silicon in tandem photovoltaic cells due to their solution processability and tunable complementary bandgaps. Herein, we show that a combination of two additives, MACl and MAH_2PO_2, in the perovskite precursor can significantly improve the grain morphology of wide-bandgap (1.64–1.70 eV) perovskite films, resulting in solar cells with increased photocurrent while reducing the open-circuit voltage deficit to 0.49–0.51 V. The addition of MACl enlarges the grain size, while MAH_2PO_2 reduces non-radiative recombination through passivation of the perovskite grain boundaries, with good synergy of functions from MACl and MAH_2PO_2. Matching the photocurrent between the two subcells in a perovskite/silicon monolithic tandem solar cell by using a bandgap of 1.64 eV for the top cell results in a high tandem V_{oc} of 1.80 V and improved power conversion efficiency of 25.4%.

INTRODUCTION

As the area-dependent balance-of-systems cost will continue to be a major cost of photovoltaic systems, power conversion efficiency (*PCE*) will remain as key driver of the levelized cost of electricity of photovoltaics.[1] The best reported *PCE* of silicon solar cells—the dominant technology in photovoltaics—has reached 26.6%,[2] close to the practical efficiency limit of approximately 27%.[2,3] This single-junction efficiency limit is mainly due to thermalization loss: the absorbed photon energy in excess of the bandgap energy is lost due to thermal relaxation of hot carriers to the band edge. To reduce the thermalization loss and thus further boost efficiency, it is necessary to engineer a silicon-based tandem solar cell technology in which a solar cell made of a wide-bandgap (WBG) material is stacked on top of the silicon cell to make more efficient use of the high-energy photons. Fortunately, silicon has a near-ideal bandgap (1.12 eV) to function as the bottom light absorber in a tandem solar cell, as predicted by the detailed-balance model.[4] Using a light absorber for the top cell with a theoretical optimal bandgap of 1.70 eV, the *PCE* of such a silicon-based tandem device can exceed 30%.[4] The challenge is to identify a top-cell partner that is efficient, cheap, and has fabrication processes that are compatible with silicon cells.

Due to their solution processability, bandgap tunability, and high photovoltaic performance without epitaxial growth that requires lattice matching, organic-inorganic halide perovskites have distinguished themselves from other photovoltaic semiconductors as suitable tandem partners for silicon.[5–18] Recent

Context & Scale

The efficiency of organic-inorganic halide perovskite solar cells skyrocketed in the past 6 years, reaching 23.3%. Their pairing with silicon in tandem solar cells offers a promising path for further reducing the levelized cost of electricity of photovoltaics. Strategies such as compositional engineering and charge-transport-layer optimization have been reported to improve the tandem efficiency. However, the large open-circuit voltage deficit of wide-bandgap perovskite cells still limits the tandem performance. Here, we utilize combined additives to smooth the perovskite film, increase its grain size, and lower its defect density. The synergistic effect of the additives leads to increased photocurrent and reduced open-circuit voltage deficit for wide-bandgap perovskite solar cells. When additives are used to form a top cell with a bandgap of 1.64 eV, the perovskite and silicon subcells are current matched and yield a perovskite/silicon tandem device with an efficiency of 25.4%.

techno-economic analyses indicate that perovskite/silicon tandem photovoltaic (PV) modules can compete with traditional silicon PV in terms of dollar-per-Watt installed cost and levelized cost of electricity if the perovskite top cell is >20% efficient, costs less than approximately $50/m^2, and has a lifetime and degradation rate comparable with that of silicon.[19,20] Different strategies have also been proposed to improve the stability of perovskite solar cells.[21–26] Several groups have reported efficient perovskite solar cells with bandgaps of 1.69–1.74 eV and PCEs of 16%–18%.[25–28] The studies on WBG perovskite solar cells mainly focus on compositional engineering for a stable phase and the selection of charge-transport layers.[25,26,28–39] With the improvement in WBG perovskite cells, the efficiencies of perovskite/silicon monolithic tandem solar cells have increased from 13.7% in 2015 to 23.6% in 2017, and to 25.2% in June 2018 (Table S1).[5–18] Optical loss, fill factor loss, current mismatch, and open-circuit voltage (V_{oc}) deficit ($E_g/q - V_{oc}$) are the main issues currently limiting the PCE of these perovskite/silicon tandem devices. Several technologies have been explored to reduce the reflection- and parasitic-absorption-induced optical losses, such as antireflective foils,[12] nanocrystalline silicon recombination junctions,[13] silicon-nanoparticle rear reflectors,[11] and double-side-textured silicon bottom cells.[15] Steps have also been taken to improve fill factor (FF): for example, the power loss caused by the large sheet resistance of the front transparent conductive oxide (TCO) electrode was reduced by introducing a metallic grid.[10,18] However, the large V_{oc} deficit remains a major hindrance for tandem devices. For example, the V_{oc} deficit of the perovskite top cell is 0.65 and 0.55 V for the tandem devices reported to achieve PCEs of 23.6% and 25.2%,[11,15] respectively, whereas the V_{oc} deficit of mature single-junction cells is typically near 0.4 V. In this study, we investigate perovskite/silicon tandem devices with different WBG perovskite solar cells, with the focus of achieving small V_{oc} deficits, large FF, and large matched sub-cell photocurrents. This is achieved via grain engineering and morphology control through the introduction of additives to the perovskite precursor.

RESULTS AND DISCUSSION

We started by fabricating efficient WBG perovskite solar cells with a bandgap of 1.70 eV, as this has been previously modeled as the ideal bandgap for perovskite/silicon tandem cells.[4] Note that, if the 1.70-eV bandgap top cell is losslessly integrated with a silicon bottom cell having a PCE of 20%, it needs to operate at 55% or 72% of its detailed-balance efficiency limit to achieve a tandem cell with a PCE of 25% or 30%, respectively.[4] We found that perovskite films deposited on silicon substrates using a precursor solution with a composition of $Cs_{0.15}(FA_{0.83}MA_{0.17})_{0.85}Pb(I_{0.7}Br_{0.3})_3$ had an optical bandgap of 1.70 eV, determined by the external quantum efficiency (EQE) edge at 728 nm (Figure S1). MACl and MAH_2PO_2 were then added to the perovskite precursor to increase the efficiency of WBG perovskite solar cells by grain engineering and defect passivation, as described in detail below. Perovskite solar cells were fabricated on indium tin oxide (ITO)/glass with poly(triaryl amine) (PTAA) as a hole-transport layer, indene C_{60} bisadduct (ICBA)/C_{60}/bathocuproine (BCP) as an electron-transport layer, and a thermally evaporated copper layer as the rear electrode. Devices with no additives in the WBG precursor solution proved capable of obtaining a PCE of 16.4% (Figure 1A). The PCE of the WBG devices then increased to ~18% when either MACl or MAH_2PO_2 additive was added, in an optimized ratio, to the precursor. After the addition of both 3 wt % MACl and 0.3 wt % MAH_2PO_2 into the precursor solution, the PCE of the WBG devices further increased to 18.6% (65% of its detailed-balance efficiency), with an improved V_{oc} of 1.19 V and short-circuit current density (J_{sc}) of

[1]Department of Mechanical and Materials Engineering, University of Nebraska-Lincoln, Lincoln, NE 68588, USA

[2]Department of Applied Physical Sciences, University of North Carolina at Chapel Hill, Chapel Hill, NC 27599, USA

[3]School of Electrical, Computer, and Energy Engineering, Arizona State University, Tempe, AZ 85287, USA
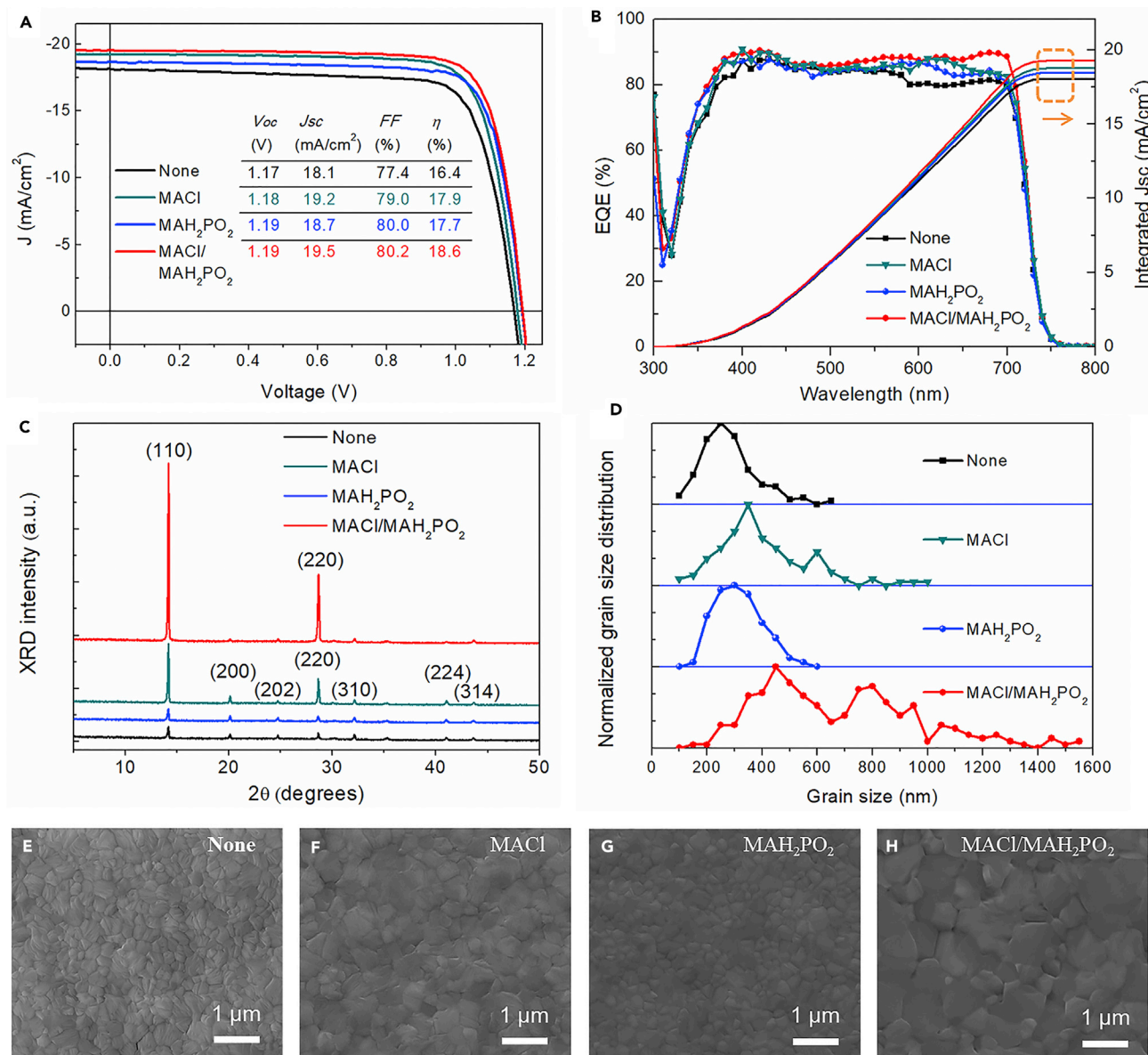
[4]Key Laboratory of Semiconductor Materials Science, Institute of Semiconductor, Chinese Academy of Sciences, Beijing, P.R. China

[5]These authors contributed equally

[6]Lead Contact

*Correspondence:
zachary.holman@asu.edu (Z.H.),
jhuang@unc.edu (J.H.)

Figure 1. High-Efficiency 1.7-eV Cs$_{0.15}$(FA$_{0.83}$MA$_{0.17}$)$_{0.85}$Pb(I$_{0.7}$Br$_{0.3}$)$_3$ Perovskite Solar Cells

(A) Device J-V curves, (B) device EQE curves and integrated J_{sc}, (C) film XRD patterns, and (D) grain size distributions. Also shown are SEM images of the perovskites fabricated from precursors (E) without additive, (F) with 3 wt % MACl additive, (G) with 0.3 wt % MAH$_2$PO$_2$ additive, and (H) with 3 wt % MACl and 0.3 wt % MAH$_2$PO$_2$ combined additive.

19.5 mA/cm^2. The EQE measurement in Figure 1B confirms the increased J_{sc} for the device based on films with combined additives compared with the device based on a pristine film. The device based on the perovskite with MACl/MAH$_2$PO$_2$ combined additives has a small V_{oc} deficit of 0.51 V, which is one of the smallest values reported for a WBG perovskite solar cell with a *PCE* above 18%.[25–28] The device *PCE* was confirmed by measuring a stable photocurrent at the maximum power point (Figure S2).

To find out why the combined additives enhance the efficiency of the WBG solar cells, we first examined the change in film morphology that they induce. Without any additives in the perovskite precursor, the films fabricated by the antisolvent
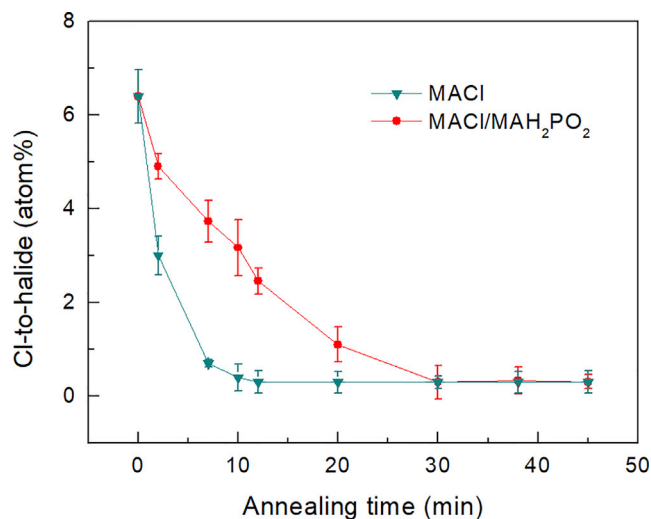
Figure 2. Impact of MAH$_2$PO$_2$ on Expelling of Chloride during Annealing

Characterization of chloride-to-halide atomic ratio for perovskite films during annealing at 100°C for different times. The perovskite films were fabricated from Cs$_{0.15}$(FA$_{0.83}$MA$_{0.17}$)$_{0.85}$Pb(I$_{0.7}$Br$_{0.3}$)$_3$ precursors with 3 wt % MACl additive alone and with 3 wt % MACl/0.3 wt % MAH$_2$PO$_2$ combined additive.

approach show a rough surface with many micrometer-sized wrinkles (Figure S3A). These wrinkles are likely formed due to substantial stress induced by the large change in lattice constant during the transformation from the intermediate phase to the perovskite phase.[40] The grain orientations are more or less random (Figure 1C). The grain size shows a unimodal distribution that can be described by a Gaussian distribution, with an average size of 250 nm (Figure 1D). After the addition of 3 wt % of MACl into the perovskite precursor, the wrinkles disappear and produce smooth WBG films with larger grains (Figures S3 and 1F). Interestingly, the grain size distribution has two peaks, at 350 and 600 nm (Figure 1D). It has been reported that MACl can slow the perovskite crystal formation process,[39,40] which allows stress to be relaxed during grain growth and thereby inhibits the formation of wrinkles. The smooth perovskite film then facilitates the formation of a more uniform electron-transport layer to create a continuous, shunt-free interconnection layer. The X-ray diffraction (XRD) (110) peak intensity increases and its full width at half maximum (FWHM) decreases after MACl is added (Figures 1C and S5). This indicates that MACl could promote growth of grains with preferential [110] orientation. This abnormal crystal growth with bimodal grain size distribution has also been reported for CH$_3$NH$_3$PbI$_{3-x}$Cl$_x$ perovskites.[41] The combination of both MACl and MAH$_2$PO$_2$ additives yields even greater improvements in grain size (Figures 1H and S4). The grain size distribution has two peaks, at 450 and 800 nm (Figure 1D), which is consistent with the further reduced FWHM of the (110) XRD peak (Figure S5). The XRD peak intensity of the (110) plane increases by three times compared with the film with only MACl additive (Figure 1C). This shows that MAH$_2$PO$_2$, in conjunction with MACl through excellent synergy, can further promote the growth of grains with preferred orientation. MACl can be expelled from the perovskite film during annealing, as revealed by previous studies.[42] Here we applied energy-dispersive spectroscopy (EDS) to track how MAH$_2$PO$_2$ affects the evaporation process of MACl during annealing, and the data are shown in Figure 2. For the perovskite film in this study with MACl additive, the Cl-to-halide atomic ratio reduces to <0.5% after annealing at 100°C for 10 min, reaching the detection limitation of EDS. For the perovskite film
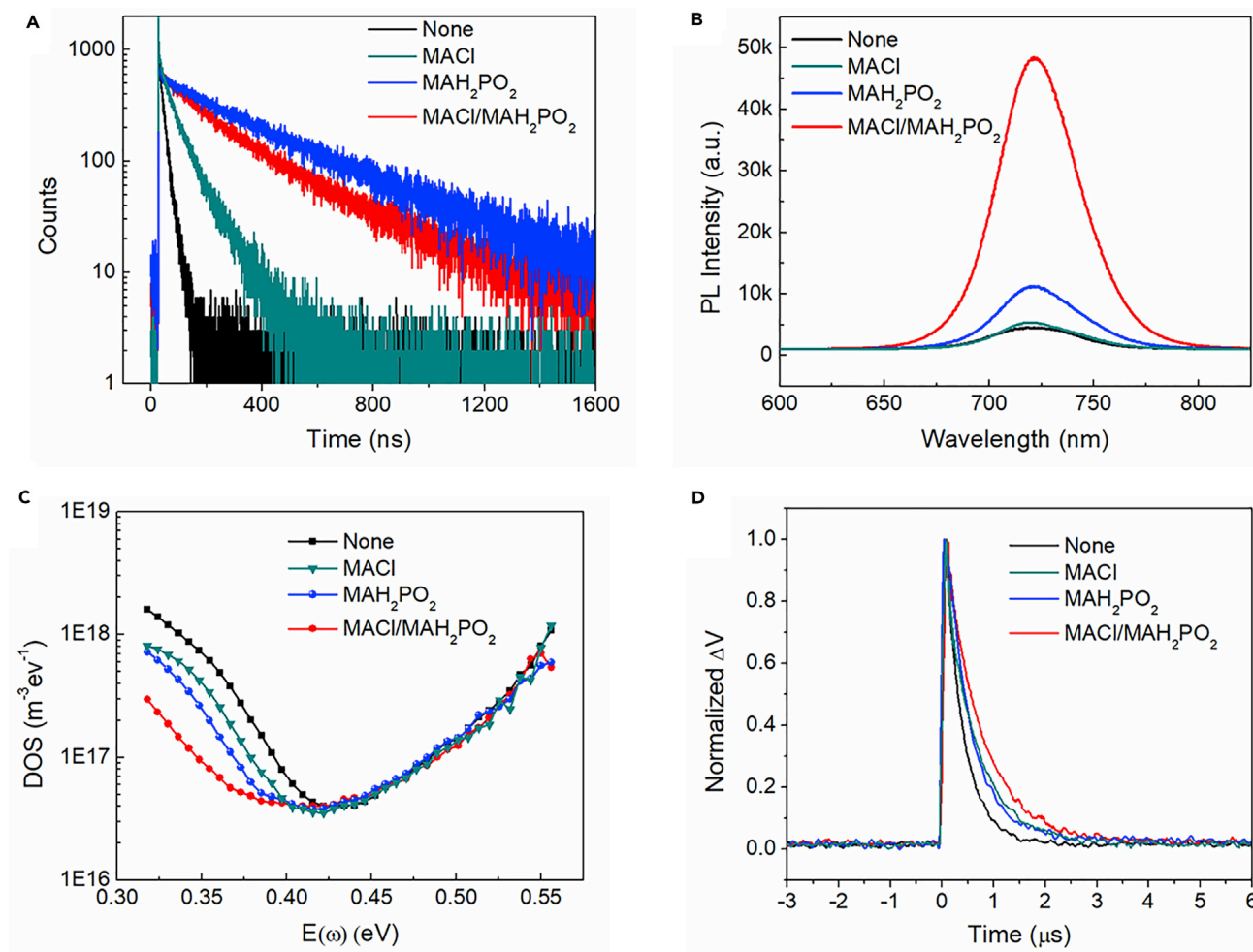
Figure 3. Impact of MACl and MAH$_2$PO$_2$ on Recombination Lifetimes and Trap Densities

(A) TRPL and (B) steady-state PL spectra of Cs$_{0.15}$(FA$_{0.83}$MA$_{0.17}$)$_{0.85}$Pb(I$_{0.7}$Br$_{0.3}$)$_3$ films deposited on glass prepared from precursor solutions without and with additives.

(C) Trap density of states obtained by thermal admittance spectroscopy and (D) transient photovoltage under AM1.5G simulated illumination and laser pulses for devices without and with additives.

with MACl/MAH$_2$PO$_2$ additives, the Cl-to-halide atom ratio is still ~3% after annealing at 100°C for 10 min. It requires approximately 30 min of annealing at 100°C for the Cl-to-halide atomic ratio to reduce to <0.5%. Therefore, MAH$_2$PO$_2$ can slow down the rate at which MACl leaves the film, thus prolonging the effect of MACl to enlarge the grain size. It should be noted that the MAH$_2$PO$_2$ additive alone does not obviously change the grain size or the XRD pattern of perovskite films (Figures 1C and 1D).

Time-resolved photoluminescence (TRPL) measurements were employed to extract charge-carrier recombination lifetimes in perovskite films with and without additives (Figure 3A). These show that MACl prolongs the carrier lifetime in the WBG perovskite films from 15 to 51 ns. This can be attributed to MACl's promotion of the growth of large grains with preferential orientation, reducing the density of grain boundaries. The addition of MAH$_2$PO$_2$ similarly increases the carrier lifetime, from 15 to 332 ns (Figure 3A), and also enhances the intensity of the steady-state photoluminescence (PL) peak (Figure 3B). We extracted the relationship between trap densities

and trap depths by thermal admittance spectroscopy in Figure 3C.[43,44] Here the energetic demarcation E(ω) is correlated with the trap depth; more details on the analysis of the trap density of states (tDOS) can be found in previous publications.[43,44] Compared with the device without any additive, that with MAH_2PO_2 has a lower tDOS in the shallower trap region (0.35–0.40 eV) but a comparable tDOS in the deeper trap region (>0.4 eV). These shallower energies are assigned to traps at the grain boundaries,[43,44] and deeper energies are assigned to defects at the film surface.[43,44] Considering the similar grain sizes of the perovskite film with MAH_2PO_2 and the pristine film, the elongated carrier lifetime and lower density of shallow traps indicate that MAH_2PO_2 can passivate the non-radiative recombination sites at the grain boundaries. As it benefits from both enlarged grains caused by the MACl additive and reduced shallow trap density caused by the MAH_2PO_2 additive, the perovskite film with the combination of MACl and MAH_2PO_2 additives has both long carrier lifetime (291 ns, Figure 3A) and strong PL intensity (Figure 3B). Transient photovoltage (TPV) measurements were performed to characterize the carrier recombination lifetimes in finished devices operating at open circuit with one-sun illumination light bias. The TPV decay curves in Figure 3D show that carrier recombination lifetime is increased from 352 to 696 ns after adding the combination of MACl and MAH_2PO_2, revealing the suppressed carrier recombination in the device. The prolonged carrier recombination lifetime should reduce the reverse-bias saturation current and increase the carrier diffusion length, enhancing the V_{oc} and J_{sc} of the perovskite device. EQE curves show that the charge extraction efficiency is increased across the whole spectral region, especially at long wavelengths, after adding combined additives. Considering that the absorption does not change appreciably with the additives (Figure S6), the improved EQE is ascribed to the reduced charge recombination.

We next fabricated a perovskite/silicon monolithic tandem device with the 1.70-eV WBG perovskite solar cell on top of a silicon heterojunction cell, with the tandem cell schematic shown in Figure 4A. ITO was used as the recombination layer to connect the perovskite top cell with the silicon bottom cell. The front surface of the silicon cell is smooth and the rear surface is textured. Figure 4B and Table 1 show the performance of the device: the *PCE* is 22.4% and, although a high V_{oc} of 1.83 V is achieved, the small J_{sc} of 16.4 mA/cm^2 limits the efficiency. There are three reasons to which we can attribute such a small J_{sc} in the perovskite cells made on silicon cells compared with the opaque device with a copper electrode made from the same precursor. First, the opaque device has a rear reflector that enables double-pass absorption of super-bandgap light, whereas the perovskite top cell in the tandem device only has single-pass absorption (Figure S7). As evident in the EQE measurements, the silicon bottom cell has 5%–40% EQE at 550–710 nm wavelengths, which generates an extra current density of 1.65 mA/cm^2 for the bottom cell that should instead go to the top cell. Second, blue parasitic absorption in indium zinc oxide (IZO) and ICBA/C60 now matters, as those layers are on the illuminated side of the device instead of on the rear (Figure S8). Lastly, the EQE edge shows a blue shift by 12 nm when the perovskite film from the same $Cs_{0.15}(FA_{0.83}MA_{0.17})_{0.85}Pb(I_{0.7}Br_{0.3})_3$ precursor solution is deposited on an ITO/silicon substrate instead of on ITO/glass (Figure S9). This substrate-dependent perovskite composition has been observed in many cases in our previous studies but is not yet understood.[45] Ellipsometry measurement and PL spectra also confirm the slight change of bandgap between perovskite films fabricated on glass substrate and on silicon substrate (Figure S10). Due to these reasons, the J_{sc} of the perovskite top cell is 3.0 mA/cm^2 smaller than that of the silicon bottom cell (Figure 4C).
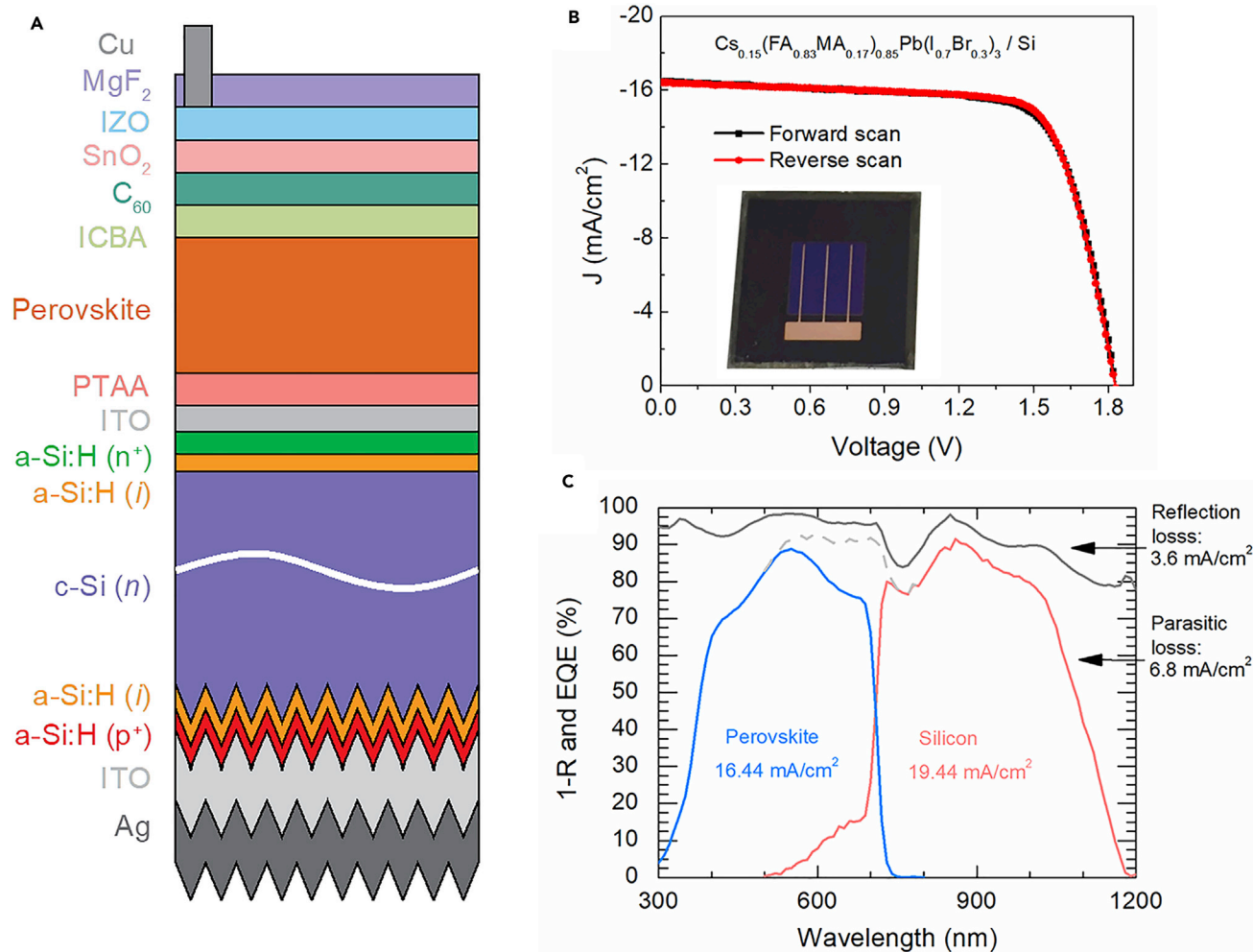
Figure 4. Perovskite/Silicon Monolithic Tandem Device with a 1.70-eV Perovskite Top Cell

(A) Schematic structure.

(B) J-V curves of $Cs_{0.15}(FA_{0.83}MA_{0.17})_{0.85}Pb(I_{0.7}Br_{0.3})_3$/Si tandem device under forward and reverse scans with an inset photograph of the tandem device.

(C) EQE and total absorbance (1-R, where R is the reflectance) of the $Cs_{0.15}(FA_{0.83}MA_{0.17})_{0.85}Pb(I_{0.7}Br_{0.3})_3$/Si tandem device.

To match the photocurrent between the sub-cells, one can either increase the thickness of the perovskite film or reduce the bandgap of the perovskite. The previously optimized $Cs_{0.15}(FA_{0.83}MA_{0.17})_{0.85}Pb(I_{0.7}Br_{0.3})_3$ device utilized a 1.35 M perovskite precursor and had an absorber thickness of ~500 nm. Thickening the absorber would seem to be the easiest option, but we found diminished device performance for thicker perovskite films due to film surface roughening and reduced charge collection efficiency. Therefore, we instead adjusted the bandgap of the perovskite top cell to increase its photocurrent. We investigated perovskite/silicon tandem devices with various bromine-to-halide atomic ratios, [Br]/([I]+[Br]), ranging from 15% to 30% in the $Cs_{0.15}(FA_{0.83}MA_{0.17})_{0.85}Pb(I_{1-x}Br_x)_3$ precursor. Reducing the ratio decreases the bandgap, and thus red-shifts the EQE edge and increases the photocurrent of the top cell. The bandgaps of perovskite films prepared from $Cs_{0.15}(FA_{0.83}MA_{0.17})_{0.85}Pb(I_{1-x}Br_x)_3$ precursors on silicon cells decrease to 1.68, 1.64, and 1.62 eV with x = 0.25, 0.20, and 0.15, respectively (Figure 5B). As with the $Cs_{0.15}(FA_{0.83}MA_{0.17})_{0.85}Pb(I_{0.7}Br_{0.3})_3$ perovskite, it is important for these precursors to have the combined MACl and MAH_2PO_2 additives to obtain better device

Table 1. Summary of Photovoltaic Parameters for the Best $Cs_{0.15}(FA_{0.83}MA_{0.17})_{0.85}Pb(I_{1-x}Br_x)_3$/Si Tandem Devices with Different [Br]/([I]+[Br]) Ratios

Device	Top-Cell Bandgap (eV)	V_{oc} (V)	J_{sc} (mA/cm^2)	FF (%)	η (%)
$Cs_{0.15}(FA_{0.83}MA_{0.17})_{0.85}Pb(I_{0.7}Br_{0.3})_3$/Si	1.70	1.83	16.4	74.5	22.4
$Cs_{0.15}(FA_{0.83}MA_{0.17})_{0.85}Pb(I_{0.75}Br_{0.25})_3$/Si	1.68	1.81	17.1	79.0	24.5
$Cs_{0.15}(FA_{0.83}MA_{0.17})_{0.85}Pb(I_{0.8}Br_{0.2})_3$/Si	1.64	1.80	17.8	79.4	25.4
$Cs_{0.15}(FA_{0.83}MA_{0.17})_{0.85}Pb(I_{0.85}Br_{0.15})_3$/Si	1.62	1.77	17.4	78.1	24.1

performance due to the smooth surfaces, larger grain size, and smaller trap density at grain boundaries (Figures S11–S15). For example, WBG perovskite solar cells based on $Cs_{0.15}(FA_{0.83}MA_{0.17})_{0.85}Pb(I_{0.8}Br_{0.2})_3$ with MACl and MAH_2PO_2 show a PCE of 19.3% and V_{oc} of 1.15 V, yielding a V_{oc} deficit of 0.49 V (Figure S15). For $Cs_{0.15}(FA_{0.83}MA_{0.17})_{0.85}Pb(I_{1-x}Br_x)_3$/silicon tandem devices, the J_{sc} increases when the [Br]/([I]+[Br]) ratio changes from 30% to 20% (Table 1). A maximum tandem J_{sc} of 17.8 mA/cm^2 is reached with 20% Br, and the EQE curves in Figure 5D confirm that the tandem is current matched with this perovskite composition. When the [Br]/([I]+[Br]) ratio is further decreased to 15%, the silicon bottom cell, instead of the perovskite cell, becomes the current-limiting cell (Figure S16), which reduces the J_{sc} of the tandem device to 17.4 mA/cm^2. As expected, the V_{oc} of $Cs_{0.15}(FA_{0.83}MA_{0.17})_{0.85}Pb(I_{1x-}Br_x)_3$/silicon tandem devices decreases with reduced [Br]/([I]+[Br]) ratio as the V_{oc} deficit remains nearly constant (Table 1).

With the optimized perovskite composition and MACl/MAH_2PO_2 as additives, the tandem cell reached a high PCE of 25.4% with a V_{oc} of 1.80 V, a J_{sc} of 17.8 mA/cm^2, and an FF of 79.4%, without notable photocurrent hysteresis (Figure 5C). The statistical distribution of the PCE is shown in Figure S17 for tandem devices with and without additives, which shows that the MACl/MAH_2PO_2 combined additives can consistently improve the photovoltaic performance of tandem devices. Unencapsulated tandem devices show good shelf stability in N_2 atmosphere with the PCE remaining at 95% of its initial value after storage for 100 days (Figure S18) and still hysteresis free (Figure S19). For the encapsulated tandem device, it retained 91.5% of its initial PCE after constant illumination of simulated AM1.5G light for 250 hours (Figure 5E). During the stability test, the device was connected to a resistor so that it worked at its maximum power point. For WBG perovskites with mixed Br and I with >30% Br among halides, phase segregation under illumination has been frequently reported as a challenge to device stability.[46–48] Several studies found that 10%–30% Cs can suppress the phase segregation of mixed halide perovskites with even 40% Br.[24,26,35,49] The WBG perovskites here contain 15% Cs and 20% Br, which enables good phase stability under illumination, as show in Figure S20.

To further increase the PCE of perovskite/silicon monolithic tandem solar cells to 30%, there are several promising approaches. First, one needs to further reduce the V_{oc} deficit for the perovskite top cell. Even though the V_{oc} deficit of 0.49 V for a 1.64-eV bandgap perovskite is small compared with other reported WBG perovskite solar cells,[50] there is still a lot of room for improvement, considering that the V_{oc} deficit is as small as 0.39 eV for perovskite solar cells with a smaller bandgap of 1.51 eV.[44] It is also crucial to reduce the parasitic absorption loss from the TCO electrode and charge-transport layers. As shown in Figure 5D, the parasitic absorption loss is as large as 5.2 mA/cm^2 for the tandem with a PCE of 25.4% (although not all of this loss can be recovered), and most of this parasitic absorption comes from the charge-transport layers and TCOs. For example, the front sputtered IZO absorbs
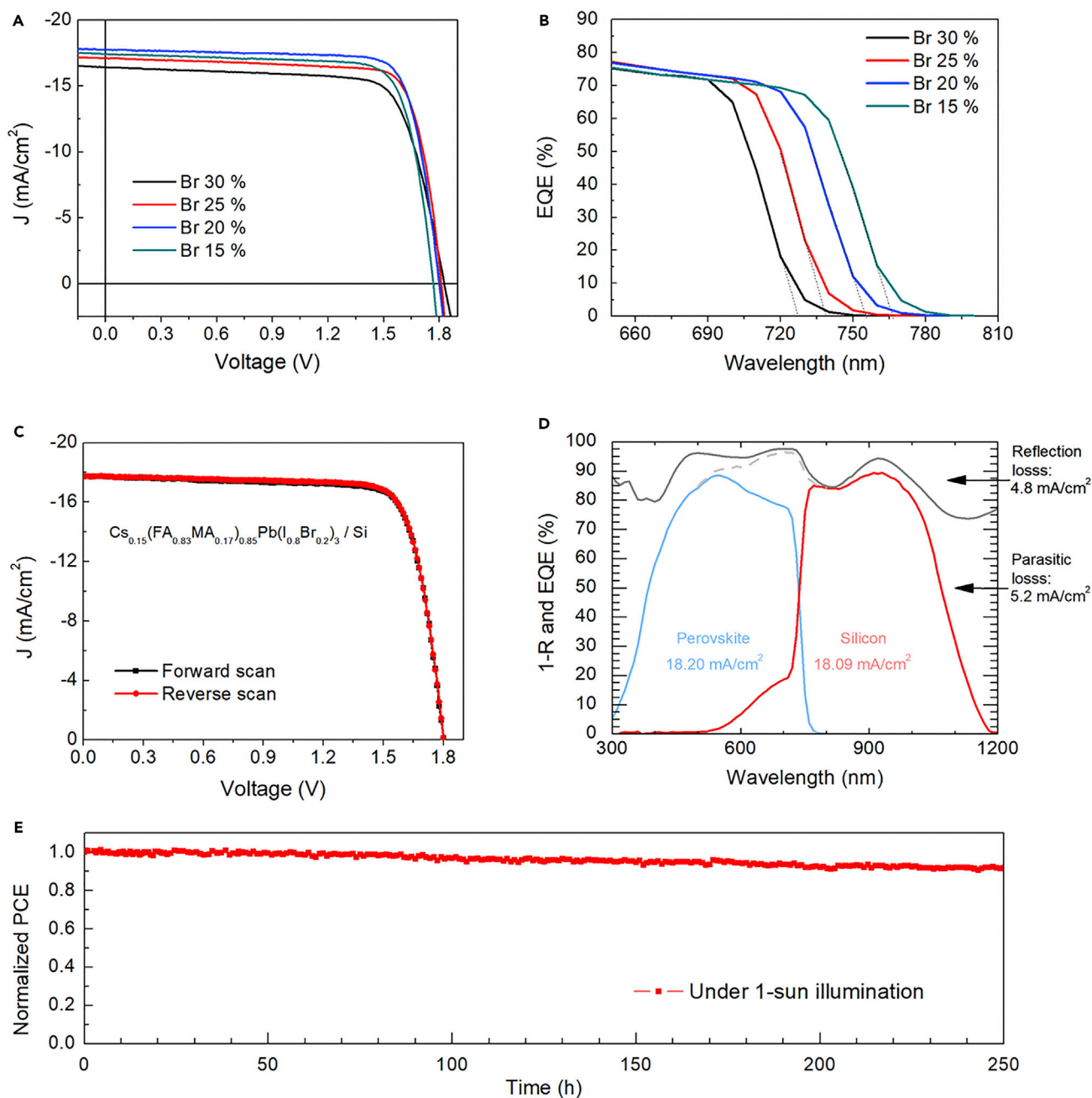
Figure 5. Perovskite/Silicon Monolithic Tandems with Different WBG Perovskite Top Cells

(A) J-V curves of different $Cs_{0.15}(FA_{0.83}MA_{0.17})_{0.85}Pb(I_{1-x}Br_x)_3$/Si tandem devices.

(B) EQE curves at the absorption edge of the perovskite top cells.

(C and D) J-V curve under forward and reverse scans (C) and EQE and 1-R of the champion $Cs_{0.15}(FA_{0.83}MA_{0.17})_{0.85}Pb(I_{0.8}Br_{0.2})_3$/Si tandem device (D).

(E) Long-term stability test of encapsulated $Cs_{0.15}(FA_{0.83}MA_{0.17})_{0.85}Pb(I_{0.8}Br_{0.2})_3$/Si tandem device under constant AM1.5G illumination at room temperature at maximum power point.

at wavelengths below 450 nm and in the near-infrared region (Figure S8), and replacing the ITO/Ag in the silicon bottom cell with a better rear reflector can further reduce the near-infrared parasitic absorption.[51] Recently, Bush et al.[18] showed that decreasing the front TCO thickness from 150 to 60 nm can reduce the optical loss, and the resulting resistive loss due to the TCO's increased sheet resistance

can be overcome by silver fingers. Lastly, the J_{sc} can also be increased by utilizing a silicon bottom cell with textured surfaces on both sides to reduce front-surface reflection losses, as demonstrated by Sahli et al.[15] It has been calculated that monolithic perovskite/silicon tandem devices can reach a matched J_{sc} as high as 20.25 mA/cm^2 with a double-side-textured silicon cell.[52] Integrating the reported synergistic effects of large grains and defect passivation with state-of-the-art optical and architecture advances provides a potential path toward 30%-efficient monolithic perovskite/silicon tandem devices.

Conclusions

In summary, grain engineering through the synergistic effect of MACl and MAH$_2$PO$_2$ additives in the perovskite precursor increases the photovoltaic performance of WBG perovskite solar cells. The addition of MACl enables preferential grain growth and large grain sizes, and thus decreases the density of grain boundaries. The addition of MAH$_2$PO$_2$ is complementary: it reduces the trap density at grain boundaries and thus reduces non-radiative recombination. The synergistic effect of MACl and MAH$_2$PO$_2$ combined additives not only retains the individual advantages of each, but also further promotes the grain growth and prolongs the carrier recombination lifetime. A smaller-than-ideal bandgap was found to be necessary to match the J_{sc} of the perovskite and silicon sub-cells in two-terminal, monolithic tandem devices. By fine-tuning the bandgap of the top perovskite cell to 1.64 eV, we achieved a 25.4%-efficient perovskite/silicon tandem device.

EXPERIMENTAL PROCEDURES

Perovskite Solar Cell Fabrication

PTAA (Sigma-Aldrich) was dissolved in toluene with a concentration of 2 mg mL^{-1} and spin coated on ITO/glass substrates at a speed of 4,000 rpm for 35 s. The spun films were then annealed at 100°C for 10 min and Cs$_{0.15}$(FA$_{0.83}$MA$_{0.17}$)$_{0.85}$Pb(I$_{1-x}$Br$_x$)$_3$ perovskite layers were fabricated by the antisolvent method. The pristine perovskite precursor solution was composed of mixed CsI, FAI, FABr, MAI, PbI$_2$, and PbBr$_2$ in the mixed solvent N,N-dimethylformamide (DMF):DMSO = 2:1, v/v, with a concentration of 1.35 M. For the perovskite precursors with additives, 3 wt % MACl or/and 0.3 wt % MAH$_2$PO$_2$ was dissolved in the precursor solution. To improve the wetting of the perovskite precursor solution on the PTAA film, the PTAA-coated ITO/glass substrate was pre-wetted by spinning 50 μL DMF at 4,000 rpm for 5 s. Then 80 μL of precursor solution was spun onto the PTAA at 2,000 rpm for 2 s and 4,000 rpm for 40 s, and the sample was quickly washed with 130 μL of toluene at the 35th s of the 4,000 rpm spin-coating process. Subsequently, the sample was annealed at 65°C for 10 min and 100°C for 15 min. ICBA (Solaris Chem) solution in 1,2-dichlorobenzene with a concentration of 20 mg mL^{-1} was coated onto the perovskite surface at 6,000 rpm for 35 s, and then annealed at 100°C for 30 min. The devices were finished by thermally evaporating C$_{60}$ (20 nm), BCP (8 nm), and Cu (80 nm) in that order.

Silicon Solar Cell Fabrication

An n-type, 250-μm-thick, double-side polished, float-zone wafer was used as the starting substrate. The wafer was textured on one side using a potassium hydroxide solution, as detailed elsewhere.[11] The wafer was cleaned in piranha, RCA-B, and buffered oxide etchant solutions prior to deposition of amorphous silicon (a-Si:H) layers. Intrinsic and p-type a-Si:H films (6 and 15 nm thick, respectively) were first deposited by plasma-enhanced chemical vapor deposition on the textured (rear) side of the wafer, and intrinsic and n-type a-Si:H films (6 and 8 nm thick, respectively) were then deposited on the polished (front) side. Detailed plasma-enhanced chemical vapor deposition

processes are published elsewhere.[53] A 20-nm-thick ITO layer was sputtered from a 90/10 In_2O_3/SnO_2 target in an MRC 944 tool on the polished side of the wafer through a shadow mask to define 7 × 7-mm-square cells. A 150-nm-thick ITO layer was also sputtered on the textured rear surface through the same shadow mask, followed by a 200-nm-thick silver layer without breaking the vacuum. The silicon cells were then annealed at 200°C for 20 min before fabricating perovskite cells on top.

Perovskite/Si Tandem Solar Cell Fabrication

The PTAA layer was spin coated on the Si bottom cell at 4,000 rpm for 35 s and then annealed at 100°C for 10 min. As above, the $Cs_{0.15}(FA_{0.83}MA_{0.17})_{0.85}Pb(I_{1-x}Br_x)_3$ perovskite layer was fabricated by the antisolvent method using a 1.35 M perovskite precursor with 3 wt % MACl and 0.3 wt % MAH_2PO_2 additive in the mixed solvent DMF:DMSO = 2:1, v:v. Subsequently, the perovskite layer was annealed at 65°C for 10 min and 100°C for 15 min. ICBA solution (20 mg mL^{-1}) in 1,2-dichlorobenzene was coated onto the perovskite surface at 6,000 rpm for 35 s and then annealed at 100°C for 30 min. Next, we thermally evaporated 20 nm of C_{60}. Then, 9 nm SnO_2 was deposited by atomic layer deposition with the following processing sequence: 0.5 s TDMASn pulse, 15 s purge (20 sccm N_2), 0.1 s deionized water pulse, and 15 s purge (20 sccm N_2). The door and body temperature was maintained at 100°C for the hot-wall reactor while the manifold temperature was 120°C with a precursor temperature of 60°C. IZO (150 nm) was sputtered on top of the SnO_2, using 30 W of RF power and a 3-inch IZO target, through a shadow mask to define 6.5 × 6.5-mm-square cells. Cu fingers (300 nm thick) with a width of 130 μm were thermally evaporated on top of the IZO layer. Finally, 150 nm of MgF_2 was thermally evaporated as an anti-reflection coating.

Device Characterization

Current-voltage measurements were recorded using a Keithley 2400 source measure unit under simulated AM1.5G irradiation (100 mW cm^{-2}), which was produced by an Xenon lamp-based solar simulator (94043A, Newport Sol3A Class AAA). The J-V measurement of the tandem device was carried out with a 6.5 × 6.5-mm photomask. The light intensity was calibrated using a 91150-KG5 silicon reference cell and meter with a KG5 window. The voltage scan rate was 0.1 V s^{-1}. The steady-state *PCE* was measured by monitoring the current at the bias voltage that gave the highest power output. For stability measurement, the perovskite/silicon tandem devices were encapsulated with Gorilla clear epoxy and a slide glass as a barrier layer in nitrogen-filled gloveboxes. XRD measurements were performed with a Rigaku D/Max-B X-ray diffractometer with Bragg-Brentano parafocusing geometry, a diffracted beam monochromator, and a conventional cobalt target X-ray tube set to 40 kV and 30 mA. Scanning electron micrographs were taken with a Quanta 200 FEG environmental scanning electron microscope. For TRPL measurement, PL of the perovskite film was triggered by a 404-nm pulsed diode laser with a pulse width of 45 ps, and the excited PL was collected by the TRPL spectroscopy (Horiba, DeltaPro). Based on the decay curve, a biexponential decay function, $y = y_0 + A_1*exp[-(x - x_0)/t_1] + A_2*exp[-(x - x_0)/t_2]$, was used to fit the decay, where t_1 is a process not related to charge recombination, which will be published elsewhere, and t_2 is trap-assisted recombination lifetime, which was used to characterize the carrier lifetime in perovskite films. Thermal admittance spectroscopy was performed using an E4980A precision LCR meter from Agilent at frequencies between 0.2 and 2,000 kHz; more details can be found in our previous study.[43] The TPV was measured under AM1.5G illumination, and a 337-nm laser pulse (SRS NL 100 Nitrogen Laser, pulse width was less than 3.5 ns) was used as a small perturbation to the background illumination on the device, and the device was serially connected to a digital oscilloscope (DOS-X 3104A) and the input impedance of the oscilloscope was

set to 1 MΩ. ΔV caused by the laser pulse was controlled to be less than 5% of the V_{oc} under light bias, the carrier lifetime was calculated based on fitting with single exponential decay function $y = y_0 + A_1{*}exp(-x/t_1)$. EQE spectra were measured using a PV measurements QE-X10 tool. When measuring perovskite top cells, the tandems were light-biased by a white light equipped with a long-pass (>800 nm) filter; when measuring silicon bottom cells, the tandems were light-biased by a blue light emitting diode. The reflectance was measured at 7° angle of incidence using a PerkinElmer Lambda 950 spectrophotometer equipped with an integrating sphere. Absorption was calculated based on the reflectance and transmittance of the sample, which were measured with the same spectrophotometer but with an Automated Reflectance/Transmittance Analyzer accessory. EDS was carried out at Hitachi S-4700 SEM with INCA PentaFETx3 from Oxford Instruments at 20 kV, the perovskite film was scraped off from ITO/glass and loaded on conductive carbon tape.

SUPPLEMENTAL INFORMATION

Supplemental Information includes 20 figures and 1 table and can be found with this article online at https://doi.org/10.1016/j.joule.2018.10.003.

AUTHOR CONTRIBUTIONS

J.H., Z.H., B.C., and Z.Y. conceived the idea. B.C. fabricated the WBG solar cells and perovskite/silicon tandem cells. Z.Y. and J.S. fabricated the silicon bottom cells. K.L. conducted the sputtering deposition and WBG solar cell fabrication. X.Z. and Y.L. synthesized the relevant chemicals. D.S. carried out ALD. P.N.R. carried out the EDS measurement. B.C., Z.Y., Z.H., and J.H. wrote the paper, and all authors reviewed the paper.

DECLARATION OF INTERESTS

The authors declare no competing interests.

REFERENCES

1. Yu, Z.J., Carpenter, J.V., III, and Holman, Z.C. (2018). Techno-economic viability of silicon-based tandem photovoltaic modules in the United States. Nat. Energy 3, 747–753.

2. Yoshikawa, K., Kawasaki, H., Yoshida, W., Irie, T., Konishi, K., Nakano, K., Uto, T., Adachi, D., Kanematsu, M., Uzu, H., and Yamamoto, K. (2017). Silicon heterojunction solar cell with interdigitated back contacts for a photoconversion efficiency over 26%. Nat. Energy 2, 17032.

3. Smith, D.D., Cousins, P., Westerberg, S., De Jesus-Tabajonda, R., Aniero, G., and Shen, Y.-C. (2014). Toward the practical limits of silicon solar cells. IEEE J. Photovolt. 4, 1465–1469.

4. Yu, Z.J., Leilaeioun, M., and Holman, Z. (2016). Selecting tandem partners for silicon solar cells. Nat. Energy 1, 16137.

5. Mailoa, J.P., Bailie, C.D., Johlin, E.C., Hoke, E.T., Akey, A.J., Nguyen, W.H., McGehee, M.D., and Buonassisi, T. (2015). A 2-terminal perovskite/silicon multijunction solar cell enabled by a silicon tunnel junction. Appl. Phys. Lett. 106, 121105.

6. Werner, J., Walter, A., Rucavado, E., Moon, S.-J., Sacchetto, D., Rienaecker, M., Peibst, R., Brendel, R., Niquille, X., and De Wolf, S. (2016). Zinc tin oxide as high-temperature stable recombination layer for mesoscopic perovskite/silicon monolithic tandem solar cells. Appl. Phys. Lett. 109, 233902.

7. Albrecht, S., Saliba, M., Baena, J.P.C., Lang, F., Kegelmann, L., Mews, M., Steier, L., Abate, A., Rappich, J., Korte, L., et al. (2016). Monolithic perovskite/silicon-heterojunction tandem solar cells processed at low temperature. Energy Environ. Sci. 9, 81–88.

8. Werner, J., Weng, C.-H., Walter, A., Fesquet, L., Seif, J.P., De Wolf, S., Niesen, B., and Ballif, C. (2016). Efficient monolithic perovskite/

silicon tandem solar cell with cell area > 1 cm^2. J. Phys. Chem. Lett. *7*, 161–166.

9. Werner, J., Barraud, L., Walter, A., Bräuninger, M., Sahli, F., Sacchetto, D., Tetreault, N., Paviet-Salomon, B., Moon, S.-J., and Allebe, C. (2016). Efficient near-infrared-transparent perovskite solar cells enabling direct comparison of 4-terminal and monolithic perovskite/silicon tandem cells. ACS Energy Lett. *1*, 474–480.

10. Sahli, F., Kamino, B.A., Werner, J., Brauninger, M., Paviet-Salomon, B., Barraud, L., Monnard, R., Seif, J.P., Tomasi, A., Jeangros, Q., et al. (2018). Improved optics in monolithic perovskite/silicon tandem solar cells with a nanocrystalline silicon recombination junction. Adv. Energy Mater. *8*, 1701609.

11. Bush, K.A., Palmstrom, A.F., Zhengshan, J.Y., Boccard, M., Cheacharoen, R., Mailoa, J.P., McMeekin, D.P., Hoye, R.L., Bailie, C.D., and Leijtens, T. (2017). 23.6%-efficient monolithic perovskite/silicon tandem solar cells with improved stability. Nat. Energy *2*, 17009.

12. Fan, R., Zhou, N., Zhang, L., Yang, R., Meng, Y., Li, L., Guo, T., Chen, Y., Xu, Z., and Zheng, G. (2017). Toward full solution processed perovskite/Si monolithic tandem solar device with PCE exceeding 20%. Solar RRL *1*, 1700149.

13. Zhu, S., Yao, X., Ren, Q., Zheng, C., Li, S., Tong, Y., Shi, B., Guo, S., Fan, L., and Ren, H. (2018). Transparent electrode for monolithic perovskite/silicon-heterojunction two-terminal tandem solar cells. Nano Energy *45*, 280–286.

14. Wu, Y.L., Yan, D., Peng, J., Duong, T., Wan, Y.M., Phang, S.P., Shen, H.P., Wu, N.D., Barugkin, C., Fu, X., et al. (2017). Monolithic perovskite/silicon-homojunction tandem solar cell with over 22% efficiency. Energy Environ. Sci. *10*, 2472–2479.

15. Sahli, F., Werner, J., Kamino, B.A., Bräuninger, M., Monnard, R., Paviet-Salomon, B., Barraud, L., Ding, L., Leon, J.J.D., and Sacchetto, D. (2018). Fully textured monolithic perovskite/silicon tandem solar cells with 25.2% power conversion efficiency. Nat. Mater. *17*, 820–826.

16. Zheng, J., Lau, C.F.J., Mehrvarz, H., Ma, F.-J., Jiang, Y., Deng, X., Soeriyadi, A., Kim, J., Zhang, M., and Hu, L. (2018). Large area efficient interface layer free monolithic perovskite/homo-junction-silicon tandem solar cell with over 20% efficiency. Energy Environ. Sci. *11*, 2432–2443.

17. Hu, J., Cheng, Q., Fan, R., and Zhou, H. (2017). Recent development of organic-inorganic perovskite-based tandem solar cells. Solar RRL *1*, 1700045.

18. Bush, K.A., Manzoor, S., Frohna, K., Yu, Z.J., Raiford, J.A., Palmstrom, A.F., Wang, H.-P., Prasanna, R., Bent, S.F., and Holman, Z.C. (2018). Minimizing current and voltage losses to reach 25%-efficient monolithic two-terminal perovskite-silicon tandem solar cells. ACS Energy Lett. *3*, 2173–2180.

19. Li, Z., Zhao, Y., Wang, X., Sun, Y., Zhao, Z., Li, Y., Zhou, H., and Chen, Q. (2018). Cost analysis of perovskite tandem photovoltaics. Joule *2*, 1559–1572.

20. Cai, M., Wu, Y., Chen, H., Yang, X., Qiang, Y., and Han, L. (2016). Cost-performance analysis of perovskite solar modules. Adv. Sci. *4*, 1600269.

21. Tan, H., Jain, A., Voznyy, O., Lan, X., de Arquer, F.P.G., Fan, J.Z., Quintero-Bermudez, R., Yuan, M., Zhang, B., and Zhao, Y. (2017). Efficient and stable solution-processed planar perovskite solar cells via contact passivation. Science *355*, 722–726.

22. Shin, S.S., Yeom, E.J., Yang, W.S., Hur, S., Kim, M.G., Im, J., Seo, J., Noh, J.H., and Seok, S.I. (2017). Colloidally prepared La-doped BaSnO$_3$ electrodes for efficient, photostable perovskite solar cells. Science *356*, 167–171.

23. Grancini, G., Roldan-Carmona, C., Zimmermann, I., Mosconi, E., Lee, X., Martineau, D., Narbey, S., Oswald, F., De Angelis, F., Graetzel, M., and Nazeeruddin, M.K. (2017). One-year stable perovskite solar cells by 2D/3D interface engineering. Nat. Commun. *8*, 15684.

24. Bush, K.A., Frohna, K., Prasanna, R., Beal, R.E., Leijtens, T., Swifter, S.A., and McGehee, M.D. (2018). Compositional engineering for efficient wide band gap perovskites with improved stability to photoinduced phase segregation. ACS Energy Lett. *3*, 428–435.

25. Hu, M., Bi, C., Yuan, Y.B., Bai, Y., and Huang, J.S. (2016). Stabilized wide bandgap MAPbBr$_x$I$_{3-x}$ perovskite by enhanced grain size and improved crystallinity. Sci. Adv. *3*, 1500301.

26. McMeekin, D.P., Sadoughi, G., Rehman, W., Eperon, G.E., Saliba, M., Hoerantner, M.T., Haghighirad, A., Sakai, N., Korte, L., Rech, B., et al. (2016). A mixed-cation lead mixed-halide perovskite absorber for tandem solar cells. Science *351*, 151–155.

27. Zhou, Y., Wang, F., Cao, Y., Wang, J.P., Fang, H.H., Loi, M.A., Zhao, N., and Wong, C.P. (2017). Benzylamine-treated wide-bandgap perovskite with high thermal-photostability and photovoltaic performance. Adv. Energy Mater. *7*, 1701048.

28. Lin, Y., Chen, B., Zhao, F., Zheng, X., Deng, Y., Shao, Y., Fang, Y., Bai, Y., Wang, C., and Huang, J. (2017). Matching charge extraction contact for wide-bandgap perovskite solar cells. Adv. Mater. *29*, 1700607.

29. Noh, J.H., Im, S.H., Heo, J.H., Mandal, T.N., and Seok, S.I. (2013). Chemical management for colorful, efficient, and stable inorganic-organic hybrid nanostructured solar cells. Nano Lett. *13*, 1764–1769.

30. Bi, C., Yuan, Y.B., Fang, Y.J., and Huang, J.S. (2015). Low-temperature fabrication of efficient wide-bandgap organolead trihalide perovskite solar cells. Adv. Energy Mater. *5*, 1401616.

31. Zhao, Y.X., and Zhu, K. (2014). Efficient planar perovskite solar cells based on 1.8 eV band gap CH$_3$NH$_3$PbI$_2$Br nanosheets via thermal decomposition. J. Am. Chem. Soc. *136*, 12241–12244.

32. Todorov, T., Gershon, T., Gunawan, O., Lee, Y.S., Sturdevant, C., Chang, L.-Y., and Guha, S. (2015). Monolithic perovskite-CIGS tandem solar cells via in situ band gap engineering. Adv. Energy Mater. *5*, 1500799.

33. Zhou, Y.Y., Yang, M.J., Game, O.S., Wu, W.W., Kwun, J., Strauss, M.A., Yan, Y.F., Huang, J.S., Zhu, K., and Padture, N.P. (2016). Manipulating crystallization of organolead mixed-halide thin films in antisolvent baths for wide-bandgap perovskite solar cells. ACS Appl. Mater. Interfaces *8*, 2232–2237.

34. Eperon, G.E., Stranks, S.D., Menelaou, C., Johnston, M.B., Herz, L.M., and Snaith, H.J. (2014). Formamidinium lead trihalide: a broadly tunable perovskite for efficient planar heterojunction solar cells. Energy Environ. Sci. *7*, 982–988.

35. Beal, R.E., Slotcavage, D.J., Leijtens, T., Bowring, A.R., Belisle, R.A., Nguyen, W.H., Burkhard, G.F., Hoke, E.T., and McGehee, M.D. (2016). Cesium lead halide perovskites with improved stability for tandem solar cells. J. Phys. Chem. Lett. *7*, 746–751.

36. Park, B.W., Philippe, B., Zhang, X.L., Rensmo, H., Boschloo, G., and Johansson, E.M.J. (2015). Bismuth based hybrid perovskites A$_3$Bi$_2$I$_9$ (A: methylammonium or cesium) for solar cell application. Adv. Mater. *27*, 6806–6813.

37. Slavney, A.H., Hu, T., Lindenberg, A.M., and Karunadasa, H.I. (2016). A bismuth-halide double perovskite with long carrier recombination lifetime for photovoltaic applications. J. Am. Chem. Soc. *138*, 2138–2141.

38. Eperon, G.E., Paternò, G.M., Sutton, R.J., Zampetti, A., Haghighirad, A.A., Cacialli, F., and Snaith, H.J. (2015). Inorganic caesium lead iodide perovskite solar cells. J. Mater. Chem. A *3*, 19688–19695.

39. Swarnkar, A., Marshall, A.R., Sanehira, E.M., Chernomordik, B.D., Moore, D.T., Christians, J.A., Chakrabarti, T., and Luther, J.M. (2016). Quantum dot-induced phase stabilization of α-CsPbI$_3$ perovskite for high-efficiency photovoltaics. Science *354*, 92–95.

40. Bush, K.A., Rolston, N., Gold-Parker, A., Manzoor, S., Hausele, J., Yu, Z.J., Raiford, J.A., Cheacharoen, R., Holman, Z.C., and Toney, M.F. (2018). Controlling thin-film stress and wrinkling during perovskite film formation. ACS Energy Lett. *3*, 1225–1232.

41. Dong, Q.F., Yuan, Y.B., Shao, Y.C., Fang, Y.J., Wang, Q., and Huang, J.S. (2015). Abnormal crystal growth in CH$_3$NH$_3$PbI$_{3-x}$Cl$_x$ using a multi-cycle solution coating process. Energy Environ. Sci. *8*, 2464–2470.

42. Chae, J., Dong, Q., Huang, J., and Centrone, A. (2015). Chloride incorporation process in CH$_3$NH$_3$PbI$_{3-x}$Cl$_x$ perovskites via nanoscale bandgap maps. Nano Lett. *15*, 8114–8121.

43. Shao, Y., Xiao, Z., Bi, C., Yuan, Y., and Huang, J. (2014). Origin and elimination of photocurrent hysteresis by fullerene passivation in CH$_3$NH$_3$PbI$_3$ planar heterojunction solar cells. Nat. Commun. *5*, 5784.

44. Zheng, X.P., Chen, B., Dai, J., Fang, Y.J., Bai, Y., Lin, Y.Z., Wei, H.T., Zeng, X.C., and Huang, J.S. (2017). Defect passivation in hybrid perovskite solar cells using quaternary ammonium halide anions and cations. Nat. Energy *2*, 17102.

45. Bi, C., Chen, B., Wei, H., DeLuca, S., and Huang, J. (2017). Efficient flexible solar cell based on composition-tailored hybrid perovskite. Adv. Mater. *29*, 1605900.

46. Hoke, E.T., Slotcavage, D.J., Dohner, E.R., Bowring, A.R., Karunadasa, H.I., and McGehee, M.D. (2015). Reversible photo-induced trap formation in mixed-halide hybrid perovskites for photovoltaics. Chem. Sci. *6*, 613–617.

47. Slotcavage, D.J., Karunadasa, H.I., and McGehee, M.D. (2016). Light-induced phase segregation in halide-perovskite absorbers. ACS Energy Lett. *1*, 1199–1205.

48. Bischak, C.G., Hetherington, C.L., Wu, H., Aloni, S., Ogletree, D.F., Limmer, D.T., and Ginsberg, N.S. (2017). Origin of reversible photoinduced phase separation in hybrid perovskites. Nano Lett. *17*, 1028–1033.

49. Rehman, W., McMeekin, D.P., Patel, J.B., Milot, R.L., Johnston, M.B., Snaith, H.J., and Herz, L.M. (2017). Photovoltaic mixed-cation lead mixed-halide perovskites: links between crystallinity, photo-stability and electronic properties. Energy Environ. Sci. *10*, 361–369.

50. Chen, B., Zheng, X.P., Bai, Y., Padture, N.P., and Huang, J.S. (2017). Progress in tandem solar cells based on hybrid organic-inorganic perovskites. Adv. Energy Mater. *7*, 1602400.

51. Boccard, M., Firth, P., Yu, Z.J., Fisher, K.C., Leilaeioun, M., Manzoor, S., and Holman, Z.C. (2017). Low-refractive-index nanoparticle interlayers to reduce parasitic absorption in metallic rear reflectors of solar cells. Phys. Status Solidi A. *214*, 1700179.

52. Santbergen, R., Mishima, R., Meguro, T., Hino, M., Uzu, H., Blanker, J., Yamamoto, K., and Zeman, M. (2016). Minimizing optical losses in monolithic perovskite/c-Si tandem solar cells with a flat top cell. Opt. Express *24*, A1288–A1299.

53. Chen, B., Bai, Y., Yu, Z., Li, T., Zheng, X., Dong, Q.F., She, L., Boccard, M., Gruverman, A., Holman, Z., and Huang, J.S. (2016). Efficient semi-transparent perovskite solar cells for 23.0%-efficiency perovskite/silicon four-terminal tandem cells. Adv. Energy Mater. *6*, 1601128.